Journal of Crystal Growth 67 (1984) 324–336
North-Holland, Amsterdam

THE THEORETICAL GROWTH MORPHOLOGY OF CALCIUM OXALATE DIHYDRATE

Wim M.M. HEIJNEN

Instituut voor Aardwetenschappen, Rijksuniversiteit Utrecht, Postbus 80021, 3508 TA Utrecht, The Netherlands

and

Frans B. VAN DUIJNEVELDT

Theoretical Chemistry Group, Rijksuniversiteit Utrecht, Padualaan 8, Utrecht, The Netherlands

Received 5 September 1983; manuscript received in final form 23 March 1984

A qualitative PBC analysis of the COD structure results in five F forms: {110}, {101}, {100}, {121} and {211}. In order to quantify the morphological importance of these forms, their attachment energies are computed in an electrostatic point charge model. This model is derived for the oxalate ion from theoretical chemical considerations and simplified for the purpose to $C_2^{+1}O_4^{-1}$. The growth forms are constructed from the attachment energies, assumed to be proportional to the growth rates. Contrary to the observed morphology, the theoretical morphology is dominated by {110}. This discrepancy can be accounted for by noting that the elementary growth layer d_{110} can be subdivided into two equivalent F slices with thickness $\frac{1}{2}d_{110}$. Both have the same slice energy, which is furthermore smaller than the d_{110} slice energy. When spiral and/or 2D growth mechanism occurs by means of both $\frac{1}{2}d_{110}$ F slices alternatingly in space and in time, the corresponding rate is higher than in the convential case of step thickness d_{110}. The presence of this growth mechanism, viewed as an extension of the original PBC theory, leads to an improved theoretical morphology in better agreement with the observed one.

1. Introduction

Calcium oxalate hydrates occur in plant tissues, as minerals of probably organic origin and in urinary calculi. The monoclinic monohydrate (whewellite, COM) is the least soluble and thermodynamically stable phase. The tetragonal dihydrate (weddellite, COD) and the triclinic trihydrate (COT) are more soluble and thermodynamically unstable under renal conditions and have therefore been studied less thoroughly [1–4]. The basic material of 63% of all uroliths is composed of calcium oxalate, of which 75% corresponds to COM and 25% to COD. Urine sediments of oxalate stone patients, however, contain nearly exclusively weddellite crystals [5]. COT is only rarely found in stones and slightly more often in crystalluria [6–8]. Many calcium oxalate stones consist of an inner core of whewellite with an outer surface layer of weddellite [6]. COD is often transformed to COM as evidenced by both polarizing microscopical observations of thin sections of urinary stones and in vitro experiments [8–10].

The morphology of weddellite crystals in human urinary calculi is determined by the tetragonal dipyramid {101}, sometimes associated with a small tetragonal prism {100} [5,8–15]. Weddellite crystals occurring in mainly marine sediments [16–21] as well as those experimentally grown from aqueous solutions or in gels have the same habit [3,4,22–26]. Although weddellite crystals from plant tissues show the same combination of forms, {101} is not always as dominant; even acicular crystals parallel to the *c*-axis have been found [26,27]. Lewis et al. [28] describe weddellite crystals from the thyroid gland of a 48-year-old woman who died of uremia; these long prismatic crystals are commonly bounded on the side by eight faces belonging to the forms {100} and {110} and are terminated by {101}.

0022-0248/84/$03.00

Which of the three hydrates will grow from a solution, as well as the morphology of the resulting phase, depends on such external factors as temperature, pH, $Ca^{2+}/C_2O_4^{2-}$ ratio, degree of supersaturation and the presence of impurities, e.g. growth inhibitors [3,7,8,26,29–33]. A high pH and a high Ca/Ox ratio are known to favour the crystallization of COD [29]. Besides those external factors, the morphology of crystals is also determined by internal ones such as the crystal structure. To be able to properly describe the influence of impurities on the morphology, one needs to know the basic appearance of a crystal in the ideal situation in which external factors are absent or do not play a role. By means of Hartman and Perdok's PBC theory [34–36], the growth form of a crystal can be derived from its crystal structure.

This has already been done in a qualitative way for weddellite by Franchini-Angela and Aquilano [23] and in more detail by Strom and Heijnen [37], but neither of them could explain satisfactorily why COD crystals normally do not show the {110} form. In order to solve this problem and to predict the growth morphology of weddellite completely, attachment energies have been calculated, from which the growth form is constructed. The results of this study are presented in the present paper.

2. Qualitative PBC analysis

2.1. Crystal structure, PBCs and F forms

The derivation of PBCs and F forms from the structure is based on cell and atomic parameters (table 1) determined by Tazzoli and Domeneghetti [38]. Since these authors located all hydrogen atoms during refinement of the crystal structure, this is an improvement with respect to Strom and Heijnen's previous PBC analysis of weddellite [37] based on a less detailed crystal structure determination by Sterling [39]. Fig. 1a shows a projection along the [001] direction. The $Ca(H_2O)_2O_6$ coordination polyhedron is presented in fig. 1b. For the PBC analysis the crystal structure is simplified and partitioned into $Ca(H_2O)_2$ and Ox subunits as described previously [7,37].

The Ca–Ox bonds can be classified in three types according to bond strength:

- A calcium is strongly bonded to an oxalate ion, if two of the oxygens belonging to the Ca coordination polyhedron form part of the considered oxalate ion.
- An oxalate group is moderately bonded to a calcium, if it contains one oxygen at an interatomic distance of 2.501 Å and another oxygen accepting a hydrogen bond from a water molecule, which is part of the calcium subunit under consideration.
- A calcium is weakly bonded to an oxalate group, if the bonding takes place exclusively by means of one water molecule in the Ca coordination polyhedron, which donates a hydrogen bond to an oxygen of the oxalate group.

All Ca–Ox bonds within one unit cell and corresponding bond lengths are given in table 2. There are eight Ox and eight $Ca(H_2O)_2$ subunits, labelled 1 to 8 in the order given by ref. [40] for the coordinates of equivalent positions.

Taking only strong and moderate bonds into account, Strom and Heijnen [37] have detected PBCs in the directions [001], $\langle \frac{111}{222} \rangle$, $\langle 100 \rangle$, $\langle 101 \rangle$ and $\langle \frac{113}{222} \rangle$. These PBCs define the F forms {110}, {101}, {200} {211} and {121}. These authors have classified {*hkl*} forms as flat (F) or nonflat (S or K) on the basis of the first encountered F configuration found in the earliest encountered PBC combination $[uvw]_1 \times [uvw]_2 = (hkl)$. How-

Table 1
Cell parameters and fractional coordinates of atomic and Ox group positions in calcium oxalate dihydrate (after Tazzoli and Domeneghetti [38]); OW indicates an oxygen atom belonging to a water molecule

Atom/group	*x*	*y*	*z*
Ca	0.1993	0.3011	0
C	0.4464	0.2415	0.1053
O(1)	0.3564	0.2458	0.1829
O(2)	0.2355	0.4634	0.1799
OW(1)	0.1490	0.1145	0
OW(2)	0.0192	0.3841	0
H(1)	0.166	0.071	0.105
H(2)	0.350	0.018	0.115
Ox	0.4464	0.2415	0
$a = 12.371$ Å,	$c = 7.357$ Å,	Space group I4/m,	$Z = 8$

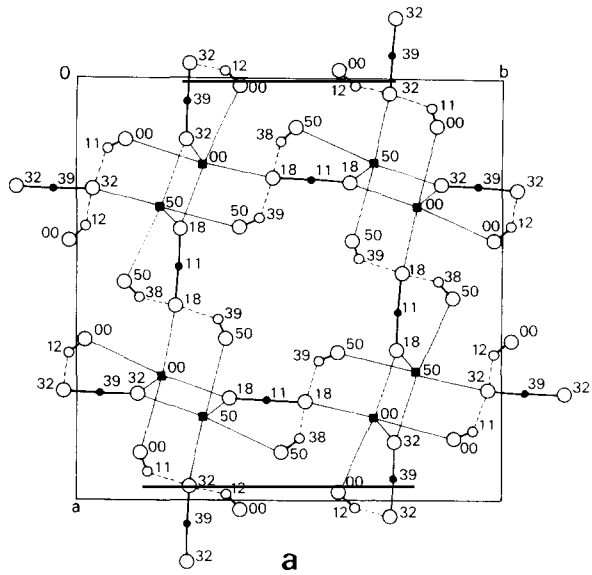

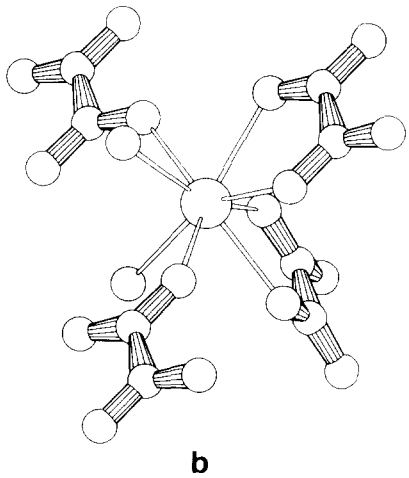

ever, they have not examined whether other F configurations are possible, arising from the combination of different pairs of PBCs parallel to (*hkl*), and hence whether other F surface profiles can be built up for the corresponding {*hkl*} form. Since the atomic distribution within a growth layer is a decisive factor for its stability, it is important to investigate the structure of the slices. Projections of the crystal structure [41] are shown parallel to the shortest PBC directions in order to visualize the different slice configurations. For clarity each $Ca(H_2O)_2$ or Ox subunit is represented by one symbol. Throughout text and figures, dashed lines refer to moderate bonds, whereas solid lines depict strong bonds.

2.2. *Projection along [001]*

The simplest primitive PBC in this direction is:

Ca1- - -Ox6- - -Ca1,001.

By enforcing on this chain the conditions of stoichiometry and electroneutrality a complete PBC, $[001]_1$, can be constructed, which is just a combination of two primitive PBCs, as shown in

Fig. 1. (a) Projection of the weddellite structure along [001]: filled squares, Ca; filled circles, C; large open circles, O; small open circles, H. Heavy solid lines are bonds within oxalate groups or water molecules; thin solid lines, strong Ca–O bonds; dashed lines, hydrogen bonds. Numbers indicate height in percent above and below the $z = 0$ plane. (b) Calcium ion surrounded by six oxygen atoms belonging to four different oxalate groups and by two water molecules.

Table 2
Calcium–oxalate bonds within the first coordination sphere in one unit cell, with bond lengths in Å; the oxalate groups are sometimes translated to neighbouring cells, as indicated by the translation indices separated by a comma from the index number

	Strong bonds		Moderate bonds		Weak bonds	
Ca1	Ox4,000	Ox1,000	Ox6,000	Ox6,00$\bar{1}$	Ox7,0$\bar{1}$0	Ox7,0$\bar{1}\bar{1}$
Ca2	Ox3,000	Ox2,000	Ox5,000	Ox5,00$\bar{1}$	Ox8,010	Ox8,01$\bar{1}$
Ca3	Ox1,000	Ox3,000	Ox8,000	0x8,00$\bar{1}$	Ox6,100	Ox6,10$\bar{1}$
Ca4	Ox2,000	Ox4,000	Ox7,000	Ox7,00$\bar{1}$	Ox5,$\bar{1}$00	Ox5,$\bar{1}$0$\bar{1}$
Ca5	Ox8,010	Ox5,000	Ox2,000	Ox2,001	Ox3,000	Ox3,001
Ca6	Ox7,0$\bar{1}$0	Ox6,000	Ox1,000	Ox1,001	Ox4,000	Ox4,001
Ca7	Ox5,$\bar{1}$00	Ox7,000	Ox4,000	Ox4,001	Ox2,000	Ox2,001
Ca8	Ox6,100	Ox8,000	Ox3,000	Ox3,001	Ox1,000	Ox1,001
Ca–Ox (Å)	3.167	3.145	4.130		5.773	

fig. 2a. Because the primitive cell contains four formula units, two Ca and two Ox subunits have to be added to the PBC $[001]_1$. This can be done in several ways. First by retaining the centre of symmetry of the PBC $[001]_1$, leading to PBCs $[001]_a$ (fig. 2b) and $[001]_b$ (fig. 2c). Both are drawn in fig. 3. In order to avoid confusion in fig. 3, the $[001]_b$ chain is translated in the direction $[\bar{1}10]$; this translation is also present in fig. 2. A second way to obtain PBCs consisting of 4 Ca and 4 Ox groups is to combine two kinds of PBCs $[001]_1$. This again can be done in two ways leading to PBCs $[001]_c$ and $[001]_d$ as shown in fig. 3.

In fig. 3 all strong and moderate bonds emanating from the constitutive groups of the PBCs are drawn. Heavy lines represent bonds within the chains; thin lines, bonds between groups belonging to different PBCs. Besides a slice d_{020}, four different slices d_{110} can be formed from the chains described. The slices $d_{110(a)}$ and $d_{110(b)}$ are different, and shifted with respect to each other by a distance $\frac{1}{2}d_{110}$. The slices $d_{110(c)}$ and $d_{110(d)}$ are symmetrically equivalent and shifted with respect to each other by a distance $\frac{1}{2}d_{110}$ and by $\frac{1}{4}d_{110}$ or $\frac{3}{4}d_{110}$ with respect to $d_{110(a)}$.

The existence of four different elementary growth layers for one F face may drastically influence its growth mechanism [42], as will be discussed in section 3.

2.3. Projection along $[\frac{1}{2}\frac{1}{2}\frac{1}{2}]$

The simplest primitive PBC in this direction consists of two Ca and two Ox groups (fig. 4):

$[\frac{1}{2}\frac{1}{2}\frac{1}{2}]_1$: Ca1—Ox4—Ca4—Ox2- - -Ca5.

This chain can be transformed into a complete PBC by adding two more Ca and Ox groups, in such a way that the resulting chain possesses no dipole moment perpendicular to its direction. The chains obtained can be divided into two groups. The first group is formed by the centrosymmetric PBCs $[\frac{1}{2}\frac{1}{2}\frac{1}{2}]_a$ and $[\frac{1}{2}\frac{1}{2}\frac{1}{2}]_b$ (fig. 4), both obtained by combining two primitive PBCs through a centre of symmetry. The second, larger group consists of complete PBCs, which are not centrosymmetric,

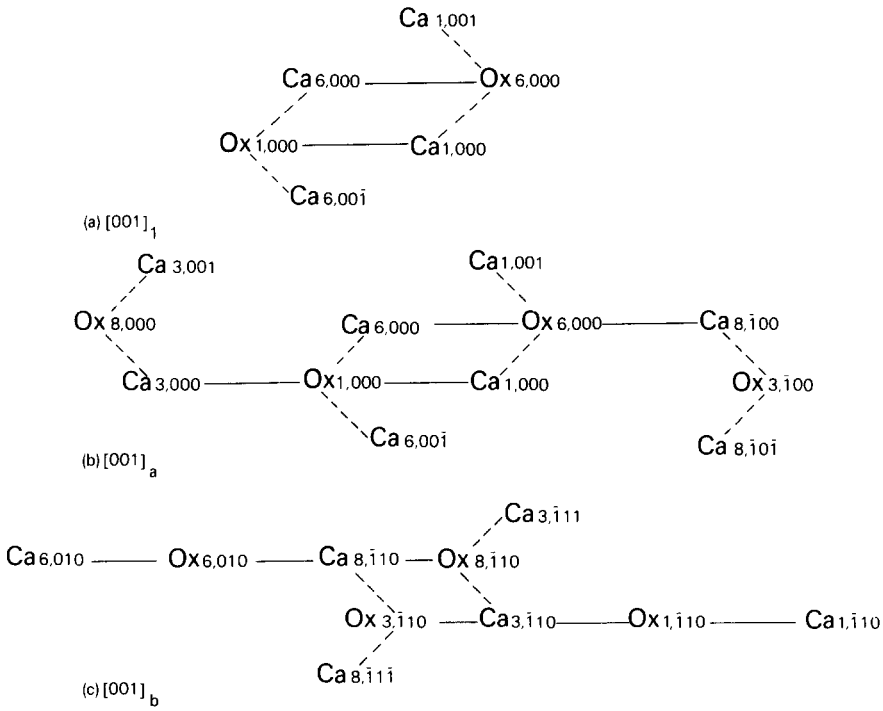

Fig. 2. Schematic configuration of PBCs ∥ [001]: solid lines are strong bonds; dashed lines, moderate bonds.

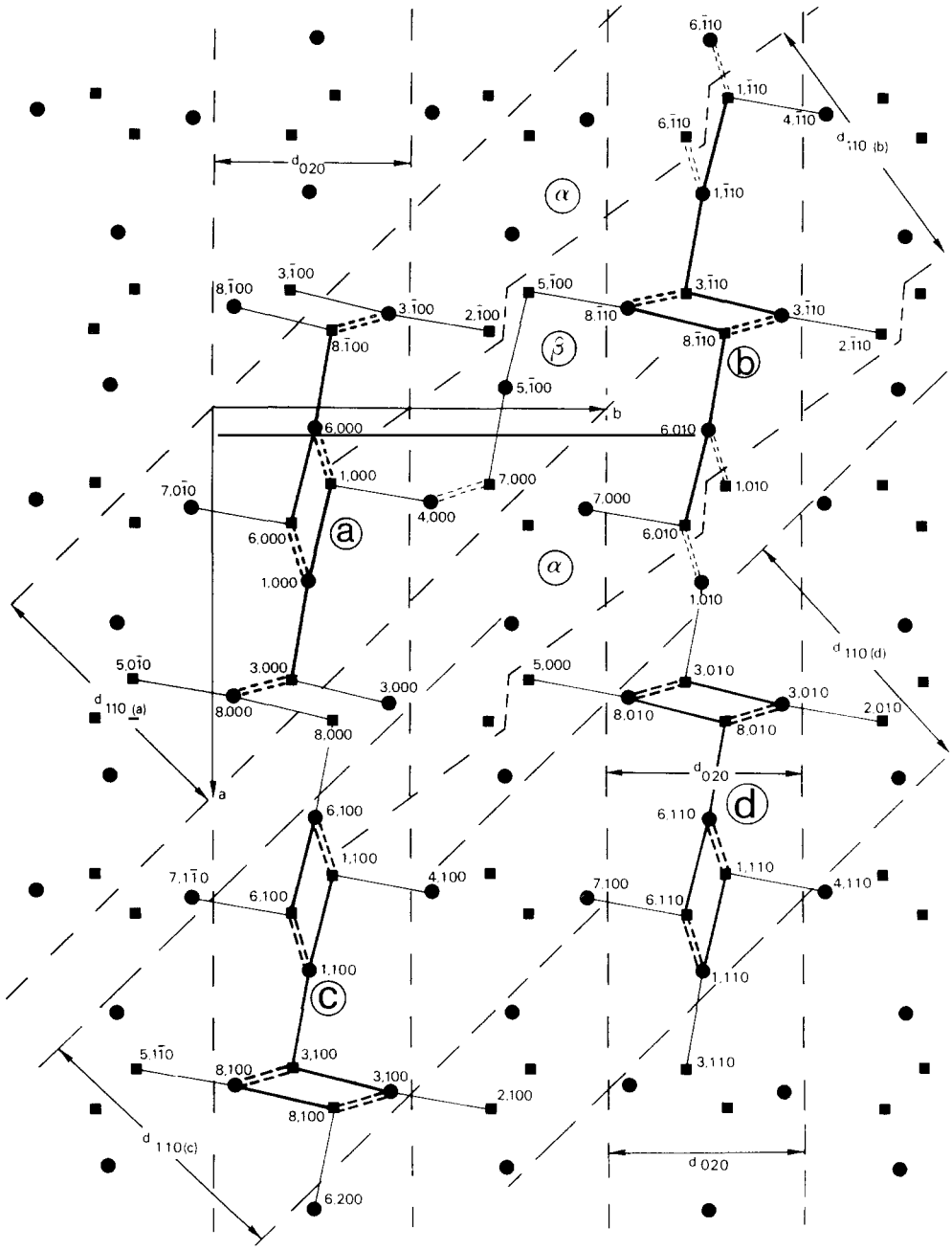

Fig. 3. Projection of the weddellite structure along [001], with PBCs $[001]_a$, $[001]_b$, $[001]_c$ and $[001]_d$ and slices d_{020} and $d_{110(a)}$, $d_{110(b)}$, $d_{110(c)}$ and $d_{110(d)}$. Solid squares are $Ca(H_2O)_2^{2+}$ subunits; solid circles, Ox^{2-} groups. Solid lines are strong bonds; dashed lines, moderate bonds; heavy lines, bonds within the PBCs; thin lines, bonds to adjacent PBCs; α and β, layers with thickness $\frac{1}{2}d_{110}$.

yet nonpolar. If a PBC search is performed by means of visual inspection of structure projections only, PBCs of this type can escape detection because of their deviating appearance. Two representatives of this second group, $[\frac{1}{2}\,\frac{1}{2}\,\frac{1}{2}]_c$ and $[\frac{1}{2}\,\frac{1}{2}\,\frac{1}{2}]_d$, are depicted in fig. 4. They are constructed from

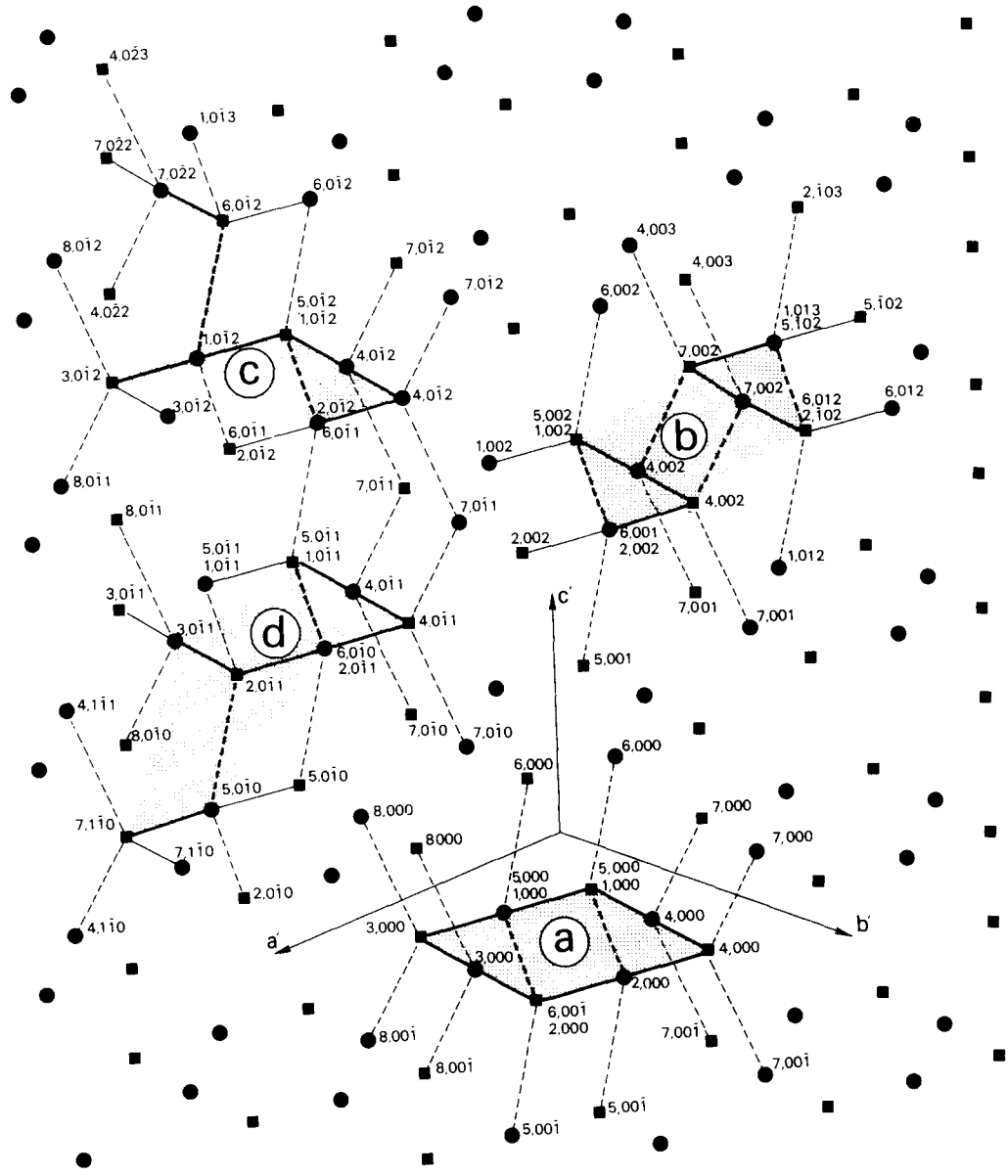

Fig. 4. Projection of the weddellite structure along $[\frac{1}{2}\frac{1}{2}\frac{1}{2}]$, with PBCs $[\frac{1}{2}\frac{1}{2}\frac{1}{2}]_a$, $[\frac{1}{2}\frac{1}{2}\frac{1}{2}]_b$, $[\frac{1}{2}\frac{1}{2}\frac{1}{2}]_c$ and $[\frac{1}{2}\frac{1}{2}\frac{1}{2}]_d$. Symbols as in fig. 3.

the $[\frac{1}{2}\frac{1}{2}\frac{1}{2}]_1$ primitive PBC by adding two Ca and two Ox. The nonpolarity is obtained by using two different centres of symmetry, one for one (Ca + Ox), the other for the second (Ca + Ox). Although more PBCs exist parallel to $[\frac{1}{2}\frac{1}{2}\frac{1}{2}]$ [37], they are not discussed here, because the four mentioned above suffice to describe all F forms.

The relative strength of the PBCs can be indicated by counting the number of strong and moderate bonds within these chains. Each crystallizing subunit is linked to four others via two strong and two moderate bonds. Since all PBCs are composed of four Ca and four Ox groups, 16 strong and 16 moderate bonds exist per PBC. The number of

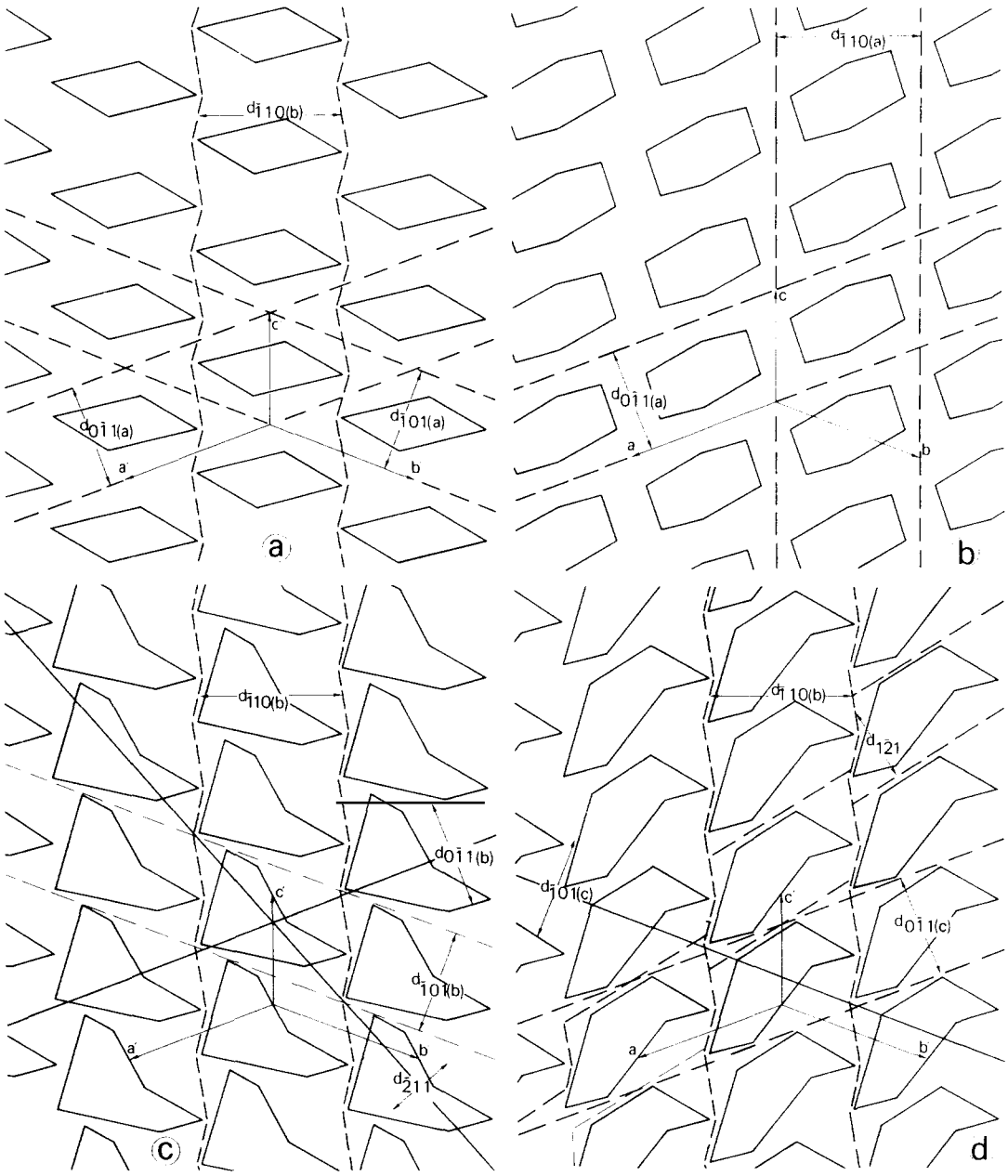

Fig. 5. Schematic projection of the weddellite structure along $[\frac{1}{2}\frac{1}{2}\frac{1}{2}]$: (a) Simplified $[\frac{1}{2}\frac{1}{2}\frac{1}{2}]_a$ PBCs and slices $d_{0\bar{1}1(a)}$, $d_{\bar{1}01(a)}$ and $d_{\bar{1}10(b)}$. (b) $[\frac{1}{2}\frac{1}{2}\frac{1}{2}]_b$ PBCs and slices $d_{0\bar{1}1(a)}$ and $d_{\bar{1}10(a)}$. (c) $[\frac{1}{2}\frac{1}{2}\frac{1}{2}]_c$ PBCs and slices $d_{0\bar{1}1(b)}$, $d_{\bar{1}01(b)}$, $d_{\bar{1}10(b)}$ and $d_{\bar{2}11}$. (d) $[\frac{1}{2}\frac{1}{2}\frac{1}{2}]_d$ PBCs and slices $d_{0\bar{1}1(c)}$, $d_{\bar{1}01(c)}$, $d_{\bar{1}10(b)}$ and $d_{1\bar{2}1}$.

bonds within each PBC is given in table 3.

Linking the above described PBCs to surrounding ones results in the F slices schematically presented in fig. 5. The PBCs in fig. 5 are represented by their simplified outlines as indicated in fig. 4. Table 3 gives the number of strong and moderate

Table 3
Number of strong and moderate bonds within a PBC or slice

PBC	Strong bonds	Moderate bonds	Slice	Strong bonds	Moderate bonds
$[\frac{1}{2}\frac{1}{2}\frac{1}{2}]_a$	16	4	$d_{\bar{1}10(a)}$	12	16
$[\frac{1}{2}\frac{1}{2}\frac{1}{2}]_b$	12	8	$d_{\bar{1}10(b)}$, $d_{0\bar{1}1(a)=\bar{1}01(a)}$	16	8
$[\frac{1}{2}\frac{1}{2}\frac{1}{2}]_c$;$[\frac{1}{2}\frac{1}{2}\frac{1}{2}]_d$	12	4	$d_{0\bar{1}1(c)=\bar{1}01(b)}$	12	8
			$d_{0\bar{1}1(b)}$, $d_{\bar{1}01(c)}, d_{\bar{2}11}$, $d_{1\bar{2}1}$	12	6

bonds within a slice per PBC.

The slices $d_{\bar{1}10(a)}$ and $d_{\bar{1}10(b)}$ are the same as found in the preceding section.

There are three slices $d_{0\bar{1}1}$ differing $\frac{1}{4}d_{0\bar{1}1}$ in level. Of these the slice $d_{0\bar{1}1(b)}$ is so highly undulated, that only a line connecting the geometric centres is drawn. Of the three slices $d_{\bar{1}01}$ two are symmetrically equivalent with $d_{0\bar{1}1}$ slices, viz.: $d_{\bar{1}01(a)} = d_{0\bar{1}1(a)}$ and $d_{\bar{1}01(b)} = d_{0\bar{1}1(c)}$. The third slice $d_{\bar{1}01(c)}$ is not equivalent to any of the $d_{0\bar{1}1}$ slices. The reason for this is that the PBCs necessary to describe such an equivalent slice were not included in the incomplete enumeration of PBCs of the second group. In conclusion it may be stated that four different slice configurations exist for the faces of the form {101}.

The slice $d_{\bar{2}11}$ has a rather elusive appearance in crystal structure projections. This explains why Franchini-Angela and Aquilano [23] considered the {121} form to be nonflat. Similarly, these authors did not detect the slice $d_{1\bar{2}1}$ belonging to the {211} form.

3. Quantitative derivation of the growth morphology

3.1. Introduction

The qualitative PBC analysis described above results in five F forms. To be able to construct the theoretical growth form, depicting the morphological importance of these forms, the relative growth rates of the different forms are required. It is however impossible to calculate these directly. However, the relative growth rate, R_{rel}, of a crystal face growing according to a layer mechanism is assumed to be proportional to its attachment energy, which in turn is a calculable quantity [43]. The attachment energy, E_{att}, is defined as minus the energy released per molecule, when a new slice with thickness d_{hkl} crystallizes on an already existing crystal face (hkl). The slice energy, E_{sl}, is minus the energy released per molecule, when a new slice d_{hkl} is formed from vapour neglecting the influence of edge energies. E_{sl} and E_{att} are complementary:

$$E_{cr} = E_{sl} + E_{att}, \tag{1}$$

where E_{cr}, the crystal energy, is defined as minus the energy released per molecule, when the crystal is formed from the crystallizing units.

Weddellite is assumed to crystallize from $C_2O_4^{2-}$ groups and $Ca(H_2O)_2^{2+}$ groups, the remainders of the $Ca(H_2O)_{6-10}^{2+}$ polyhedra present in solution [44]. Since weddellite is an ionic crystal the energies can be computed using the Madelung method [34,35,45,46] for calculating electrostatic potentials in a point charge model. All computations have been performed with the Fortran IV programme ENERGY, developed by Woensdregt [47]. The transformation factor from e^2 Å^{-1} into kJ mol^{-1} has been taken as 1389.345. On the basis of the calculated attachment energies the theoretical growth form can be constructed by Wulff's method [48], taking the central distances, defined

as the lengths of the normals from the origin to the crystal faces, directly proportional to $|E_{att}|$. Strom's [49] APL programmes CRYSTALFORM and CRYSTALDRAW have been used to obtain three-dimensional Wulff plots.

3.2. Point charge model for weddellite

Theoretical chemical studies on the charge distribution in complex anions like CO_3^{2-} [50,51], ClO_4^-, SO_4^{2-} and PO_4^{3-} [52], result in effective charges of the oxygen atoms varying in the range -0.44 to -1.05 e. For that reason we concluded that a realistic point charge model for the oxalate anion should not be completely ionic. Since, however, no such model has to our knowledge ever been published, we have arrived at the following model. An electronic wave function was obtained in the LCAO–MO–SCF approximation. These calculations were carried out using a local version of the IBMOLH programme system [53]. A double zeta (9,5) → [4,2] Gaussian basis set was used, with exponents taken from ref. [54]. The nuclear framework (fig. 6) has the geometry as reported by Tazzoli and Domeneghetti [38], which has mm2 rather than the full mmm symmetry. This dissymetry showed up in a small nonzero dipole moment μ_y of 0.21×10^{-30} C m (calculated at centre of mass, $Y_{cm} = +0.0017$ Å). Thus in the point charge model we assign a charge $-(q + 0.004)$ e to 01 and 02, and a charge of $-(q - 0.004)$ e to 03 and 04. The quadrupole moments calculated from the wave function allow us to determine q as well as a second parameter. The latter was chosen to be the distance (Δ) of the remaining charges $(2q - 1)$ from C1 in the $+x$ and from C2 in the $-x$ directions, respectively.

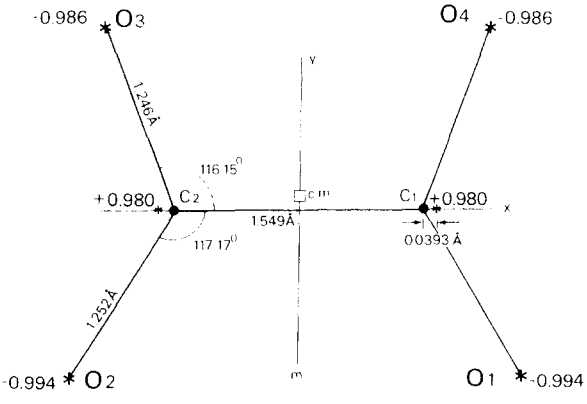

Fig. 6. Schematic presentation of the point charge model for the oxalate anion in the weddellite structure; cm is centre of mass; m indicates a mirror plane.

The values of q and Δ were then determined by equating the quadrupole moments of the point charge model, viz.

$$Q_{xx} = \sum_i q_i \left(x_i^2 - \tfrac{1}{2} y_i^2 \right), \tag{2}$$

$$Q_{yy} = \sum_i q_i \left(y_i^2 - \tfrac{1}{2} x_i^2 \right), \tag{3}$$

to the expectation values obtained from the wave function, viz. $Q_{xx} = -52.761$ and $Q_{yy} = -32.888 \times 10^{-40}$ C m^2 (at centre of mass). In this way we find $q = 0.990$ e and $\Delta = 0.0393$ Å. The resulting charge model is shown in fig. 6. It may be noted that the final charges are qualitatively similar, but quantitatively very different from the net charges that may be estimated from the Mulliken populations, viz.

$q_{O1} = q_{O2} = -0.667$ e, $q_{O3} = q_{O4} = -0.657$ e,

$q_C = +0.324$ e.

In the following electrostatic energy calculations a simplified point charge model for the oxalate ion has been used, with effective charges of $-$e on the oxygen sites and $+$e on the carbon sites, for the sake of simplifying the computations. This slight deviation from the theoretically developed model is justified, because it lies well within the margin of other at least as rough approximations, e.g.: taking R_{rel} directly proportional to E_{att}; neglecting other energy parameters than Coulomb interaction, e.g. those due to dispersion and repulsion; supposing the atomic configuration of the outermost layer of a growing crystal to be identical with the bulk crystal structure; neglecting the effects of the solution from which weddellite crystallizes, by assuming the crystal to be formed from vapour. Using this simplified model and taking a normal charge of $+2$ e on the Ca sites, the energy computations have been carried out for three different charge distributions within the water molecules, namely H^0, $H^{+1/2}$ and H^{+1}. As a matter of

course the effective charge on the oxygen atoms belonging to the water molecules is simultaneously adjusted to OW^0, OW^{-1} and OW^{-2}, respectively.

3.3. The growth form of weddellite

Table 4 shows the calculated attachment energies of the various slices for the three different point charge models used. For all, except the d_{020} and the $d_{110(c)}$ slice configurations E_{att} increases with increasing charge on the hydrogen atoms. This is due to the position of part of the water molecules, which lie at the outermost boundary of most slices. The d_{020} and the $d_{110(c)}$ slices do not contain such protruding water molecules, as can be seen in figs. 1a and 3. The crystal energy, on the contrary, decreases with increasing charge on the hydrogen atoms (table 4). To obtain the crystal energies from the calculated potentials in the present point charge models, corrections have to be made for the Coulomb interactions within the crystallizing units. The same holds for the slice energy, but of course not for the attachment energy, since a slice does not share crystallizing units with underlying slices.

Assuming a crystal face, for which more than one slice configuration is possible, to grow via the slice with the smallest E_{att}, the theoretical growth form has been constructed for the three different charge distributions. In contrast with the usually observed morphology, described in section 1, the theoretical growth morphology, as presented in figs. 7a–7c, appears to be dominated by {110}. The orthographic crystal drawings [49] in fig. 7 are projections of the crystal in the [310] direction and the crystals are of equal volumes. The forms {211} and {121} have too high attachment energies to appear on any of the crystals, whereas the tetragonal prism {100} is only present in the H^{+1} model (fig. 7c).

Table 4
Attachment energies, crystal energies and $E_{cr} - E_{sl}(\alpha)_{110}$ for the three different charge distribution models

Face	Energy (kJ/mol)		
	H^0	$H^{+1/2}$	H^{+1}
110(a)	−119.7	−147.7	−195.0
110(b)	−215.3	−285.3	−370.3
110(c)	−212.6	−195.0	−182.5
020	−264.4	−239.2	−207.4
$0\bar{1}1$(a)	−164.8	−205.9	−254.4
$0\bar{1}1$(b)	−495.2	−541.5	−586.2
$0\bar{1}1$(c)	−391.7	−397.9	−422.7
$\bar{1}01$(c)	−494.3	−567.2	−646.4
$\bar{2}11$	−498.2	−569.1	−651.3
$1\bar{2}1$	−479.0	−511.0	−546.4
E_{cr}	−2755.5	−2701.5	−2667.6
$E_{cr} - E_{sl}(\alpha)_{110}$	−333.8	−438.6	−562.0

Hartman and Heijnen [42] recently reported similar discrepancies between calculated and observed morphologies encountered in deriving the theoretical habits for aragonite, barite, zircon, ADP and KDP. Some forms {*hkl*}, e.g. {110} in the case of weddellite, were rather prominent on the theoretical habit, while on the observed habits they were much less pronounced or even absent. Apparently, in all cases two elementary growth layers A and B are possible, differing in level by $\frac{1}{2}d_{hkl}$. Moreover, each of the layers A and B, e.g. $d_{110(a)}$ and $d_{110(b)}$ for weddellite, could be split up into two layers α and β, each with thickness $\frac{1}{2}d_{hkl}$, having a stoichiometric composition. These thinner layers by themselves contain partial [55] or complete PBCs in at least two directions, so that they could be considered as slices of an F face.

For the weddellite (110) face, the four different growth layers are drawn in fig. 3. In between the PBCs $[001]_a$ and $[001]_b$ in fig. 3 the slices $d_{110(a)}$ and $d_{110(b)}$ partly overlap, defining a layer with thickness $\frac{1}{2}d_{110}$. Within this layer β three partial PBCs, having an electrostatic dipole moment perpendicular to the chain direction, are present:

$\left[\bar{\tfrac{1}{2}}\tfrac{1}{2}\tfrac{1}{2}\right]$: Ca1—Ox4- - -Ca7—Ox5,$\bar{1}$00—Ca5,$\bar{1}$00,

$\left[\bar{\tfrac{1}{2}}\tfrac{1}{2}\bar{\tfrac{1}{2}}\right]$: Ca1—Ox4- - -Ca7,00$\bar{1}$—Ox5,$\bar{1}0\bar{1}$—Ca5,$\bar{1}0\bar{1}$,

[00$\bar{1}$]: Ca7- - -Ox4- - -Ca7,00$\bar{1}$.

Since the central lines as well as the boundaries of both d_{110} slices run through centres of symmetry, the two different layers α and β (fig. 3) with thickness $\frac{1}{2}d_{110}$ are symmetrically equivalent. They have, however, opposite electrostatic dipole moments. Since only the growth layer of thickness $\frac{1}{2}d_{110}$ and not the crystal structure as a whole is

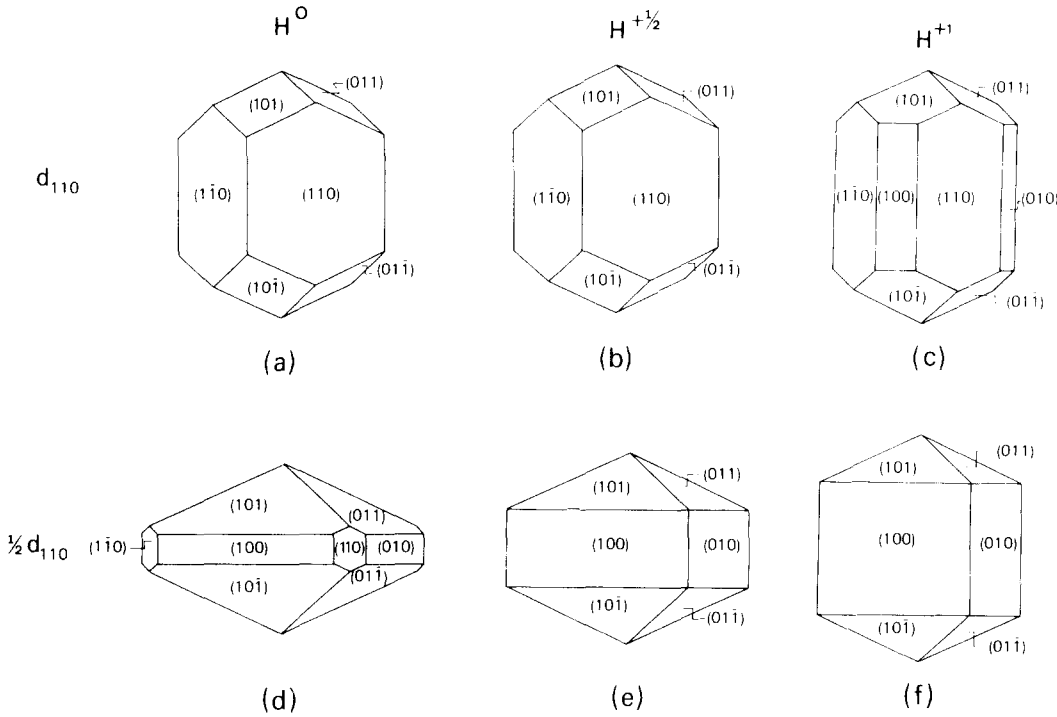

Fig. 7. Growth forms of weddellite for the three different charge distributions H^0, $H^{+1/2}$ and H^{+1}: (a–c) assuming that faces of the form {110} grow via slices d_{110}; (d–e) taking halving of the d_{110} slices into account.

polar and because the growing crystal is in contact with an aqueous solution and not with vacuum, we assume that surface restructuring can be neglected. It should be pointed out here explicitly that this situation is completely different from that found on the (111) face of NaCl, where the polar layer is stacked upon similar layers, so that the cooperation effect of all dipole moments will lead to a restructuring. In the case discussed here the polar layer rests on a layer with double height having no dipole moment. So the energy gain for restructuring would be of the same order of magnitude as for a nonpolar slice. The results obtained by 't Hart [55] show that surface restructuring can be safely ignored.

The slices α and β grow alternatingly both in space and in time. Because $E_{sl}(\alpha) = E_{sl}(\beta)$ is smaller than $E_{sl}(d_{110(a)})$ or $E_{sl}(d_{110(b)})$, the growth rate $R_{110}(\alpha)$, now assumed to be proportional to $(E_{cr} - E_{sl}(\alpha))$, listed in table 4, is higher than $R_{110}(d_{110(a)})$ or $R_{110}(d_{110(b)})$. On the contrary, the $d_{110(c)}$ and $d_{110(d)}$ slices cannot be split up into two halved layers with F character.

Taking this halving of the d_{110} slices into account, revised growth forms have been constructed. Figs. 7d–7f show the resulting growth morphologies for the three different charge distributions, drawn at the same volume as figs. 7a–7c. The increasing importance of {100} with increasing charge on the hydrogen atoms is again remarkably noticeable. Assuming the $H^{+1/2}$ model to be close to reality, we find a fair agreement between the theoretical and the observed habit of weddellite.

Hartman and Heijnen [42] also discussed the possibility that two slice configurations may be present, differing in level by $\frac{1}{2}d_{hkl}$, but such that the resulting layers with thickness $\frac{1}{2}d_{hkl}$ do not have the character of an F slice. Growth would then occur simultaneously by means of slices A and B with thickness d_{hkl}, in which case the layers A and B would form different domains on a face.

The boundary between two domains is a non-moving step with fractional height $\frac{1}{2}d_{hkl}$, at wich two-dimensional nucleation is made easier, resulting in an increased growth rate. The relative areas of the domains depend on the surface energies.

In section 2.3 of the present paper we have shown four different slice configuration for the {101} F form of weddellite. The surface energies per mole, with reference to vacuum, E_s, are given in table 5 for the $H^{+1/2}$ model. The specific surface free energies γ, again with reference to vacuum, can be calculated from:

$$\gamma = Z_p d_{hkl} E_s / 2V_p N_A, \tag{4}$$

where Z_p is the number of molecules per primitive cell; V_p is the volume of the primitive cell and N_A is Avogadro's number. The resulting γ for the most stable configuration, i.e. $d_{0\bar{1}1(a)}$, is 768 mJ m^{-2}. For sparingly soluble salts the specific surface free energy with reference to a surrounding aqueous solution is however of the order of 100 mJ m^{-2}, which is 0.13 times the calculated γ. We assume that the same correction factor can be applied to the surface energies per mole, leading to $E'_s = 0.13E_s$. Assuming a Boltzmann type of distribution, the relative areas x_i are:

$$x_i = \exp\left(E'_{s(i)}/RT\right) / \sum_{i=1}^{4} \exp\left(E'_{s(i)}/RT\right). \tag{5}$$

Taking $RT = 2.5$ kJ mol^{-1} the relative areas have been calculated and are given in table 5. The domain having the $d_{0\bar{1}1(a)}$ slice configuration appears to cover the surface of the faces of the {101} form completely. Thus there are no boundaries between different domains, and therefore no increase in growth rate due to fractional steps [42]. The growth forms depicted in fig. 7d–7f can thus serve as the conclusion of the present paper.

Table 5
Surface energy per mole E_s and relative surface area x_i of the {101} faces for the different slice configurations when the charge distribution of the water molecule is $H^{+1/2}$, OW^{-1}

i	Slice	E_s (kJ/mol)	x_i
1	$0\bar{1}1$(a)	−206	1
2	$0\bar{1}1$(b)	−595	0
3	$0\bar{1}1$(c)	−398	0
4	$\bar{1}01$(c)	−646	0

Acknowledgements

We are greatly indebted to Professor Dr. P. Hartman for many stimulating discussions and for his constructive criticism of the manuscript. We are grateful to Drs. C.F. Woensdregt for use of the computer programmes ENERGY and CRYPRO and for his ever present help. We are thankful to Dr. C.S. Strom for correcting the English and for putting her computer programmes CRYSTALFORM and CRYSTALDRAW at our disposal. We further wish to thank Mr. J.H. Bliek, Mr. W.J.J. Smeets and Mr. J.R. Meye for making the drawings.

References

[1] B. Tomazic and G.H. Nancollas, J. Crystal Growth 46 (1979) 355.
[2] B. Tomazic and G.H. Nancollas, Invest. Urol. 16 (1979) 329.
[3] B. Tomazic and G.H. Nancollas, J. Colloid Interface Sci. 75 (1980) 149.
[4] B. Tomazic and G.H. Nancollas, Invest. Urol. 18 (1980) 97.
[5] W. Berg, J.D. Schnapp, H.J. Schneider, A. Hesse and E. Hienzsch, Eur. Urol. 2 (1976) 92.
[6] E.L. Prien, J. Urol. 89 (1963) 917.
[7] W.M.M. Heijnen, J. Crystal Growth 57 (1982) 216.
[8] A. Schaefer and W. Dosch, in: Pathogenese und Klinik der Harnsteine, Vol. VI, Eds. W. Vahlensieck and G. Gasser (Steinkopff, Darmstadt, 1978) p. 110.
[9] G. Schubert and G. Brien, in: Pathogenese und Klinik der Harnsteine, Vol. VI, Eds. W. Vahlensieck and G. Gasser (Steinkopff, Darmstadt, 1978) p. 124.
[10] W. Berg, P. Lange, C. Bothor and D. Roessler, Eur. Urol. 5 (1979) 136.
[11] R.I. Gibson, Am. Mineralogist 59 (1974) 1177.
[12] L.J.M.J. Blomen, Fortschr. Urol. Nephrol. 17 (1981) 216.
[13] L.J.M.J. Blomen, Thesis, Leiden (1982).
[14] K.M. Kim and F.B. Johnson, in: Scanning Electron Microscopy/1981, Ed. O. Johari (SEM, AMF O'Hare, IL) p. 147.
[15] P.G. Werness, J.H. Bergert and L.H. Smith, J. Crystal Growth 53 (1981) 166.
[16] F.A. Bannister and M.H. Hey, Discovery Rept. 13 (1936) 60.

[17] C.O. Hutton and W.H. Taft, Mineral. Mag. 34 (1965) 256.
[18] H.A. Lowenstam, Science 162 (1968) 1129.
[19] J.I. Marlowe, J. Sediment. Petrol. 40 (1970) 499.
[20] W.C. Graustein, K. Cromack and P. Sollins, Science 198 (1977) 1252.
[21] G.J. van der Lingen, Sedimentology 26 (1979) 731.
[22] P.G. Werness, S.C. Duckworth and L.H. Smith, Invest. Urol. 17 (1979) 230.
[23] M. Franchini-Angela and D. Aquilano, J. Crystal Growth 47 (1979) 719.
[24] S. Bisaillon and R. Tawashi, J. Pharm. Sci. 64 (1975) 458.
[25] H.A. Klasens, W. G. Perdok and P. Terpstra, Z. Krist. 96 (1937) 227.
[26] A. Frey-Wyssling, Am. J. Botany 68 (1981) 130.
[27] D.W. Jackson, in: Scanning Electron Microscopy/1981, Ed. O. Johari (SEM, AMF O'Hare, IL) p. 279.
[28] R.D. Lewis, H.A. Lowenstam and G.R. Rossman, Arch. Pathol. 98 (1974) 149.
[29] J. Laniepce, Thesis, Caen (1966);
L. Walter-Lévy and J. Laniepce, Compt. Rend. (Paris) 254 (1962) 296.
[30] G. Scurfield, A.J. Michell and S.R. Silva, Bot. J. Linnean Soc. 66 (1973) 277.
[31] D.J. Sutor, Brit. J. Urol. 41 (1969) 171.
[32] D.J. Sutor and S.E. Wooley, Brit. J. Urol. 42 (1970) 296.
[33] W. Wunderlich, Urol. Res. 9 (1981) 157.
[34] P. Hartman and W.G. Perdok, Acta Cryst. 8 (1955) 49.
[35] P. Hartman, in: Crystal Growth: An Introduction, Ed. P. Hartman (North-Holland, Amsterdam, 1973) ch. 14.
[36] P. Hartman, Forschr. Mineral. 57 (1979) 127.
[37] C.S. Strom and W.M.M. Heijnen, J. Crystal Growth 51 (1981) 534.
[38] V. Tazzoli and C. Domeneghetti, Am. Mineralogist 65 (1980) 327.
[39] C. Sterling, Acta Cryst. 18 (1965) 917.
[40] International Tables for X-ray Crystallography, Vol. I, Eds. N.F.M. Henry and K. Lonsdale (Kynock, Birmingham, 1952) S.G. 87.
[41] C.F. Woensdregt, Geol. Mineral. Inst., Leiden State University, internal report (1970).
[42] P. Hartman and W.M.M. Heijnen, J. Crystal Growth 63 (1983) 261.
[43] P. Hartman and P. Bennema, J. Crystal Growth 49 (1980) 145.
[44] N.A. Hewish, G.W. Neilson and J.E. Enderby, Nature 297 (1982) 138.
[45] E. Madelung, Physik. Z. 19 (1918) 524.
[46] W. Kleber, Neues Jahrb. Mineral. Geol. Palaeontol. Beil. A75 (1939) 72.
[47] C.F. Woensdregt, Geol. Mineral. Inst., Leiden State University, internal report (1971).
[48] G. Wulff, Z. Krist. Mineral. 34 (1901) 499.
[49] C.S. Strom, J. Crystal Growth 46 (1979) 185.
[50] P.S. Yuen, M.W. Lister and S.C. Nyburg, J. Chem. Phys. 68 (1978) 1936.
[51] H.D.B. Jenkins, K.F. Pratt, B.T. Smith and T.C. Waddington, J. Inorg. Nucl. Chem. 38 (1976) 371.
[52] H. Johansen, Theoret. Chim. Acta 32 (1974) 273.
[53] CDC-IBMOLH, Theoretical Chemistry Group, Utrecht, internal report (1976).
[54] J.G.C.M. van Duijneveldt-van de Rijdt and F.B. van Duijneveldt, J. Mol. Struct. 89 (1982) 185.
[55] J. 't Hart, Can. Mineralogist 16 (1978) 175;
J. 't Hart, Thesis, Leiden (1978).